ACS MATERIALS LETTERS

www.acsmaterialsletters.org

Quantifying Local Heterogeneities in the 3D Morphology of X-PVMPT Battery Electrodes Based on FIB-SEM Measurements

Published as part of ACS Materials Letters special issue "Post-Lithium Battery Materials".

Lukas Dodell,[▽] Matthias Neumann,*[,▽] Markus Osenberg, André Hilger, Gauthier Studer, Birgit Esser, Ingo Manke, and Volker Schmidt

Cite This: ACS Materials Lett. 2025, 7, 1914–1921

Read Online

ACCESS | Metrics & More | Article Recommendations | Supporting Information

ABSTRACT: **Organic electrode-active materials (OAMs) enable a variety of charge and storage mechanisms and are advantageous compared with lithium-ion batteries in terms of costs and safety. Cross-linked poly(3-vinyl-*N*-methylphenothiazine) (X-PVMPT) is a p-type OAM showing high performance and enabling fast and reversible energy storage in different battery configurations. Beyond its molecular or polymer structure, the performance of an OAM depends strongly on the structure of the composite electrode. The porous nanostructure of an electrode composed of X-PVMPT, a conductive carbon additive, and binder is statistically investigated based on highly resolved 3D image data. Univariate probability distributions of relevant morphological descriptors and bivariate distributions of pairs of such descriptors are parametrically modeled. In this way, local heterogeneities and spatial gradients are quantified. While the observed short transportation paths through the solid phase are beneficial in terms of electrical conductivity, the pathways through the pore phase influencing the effective ionic diffusivity are comparatively long.**

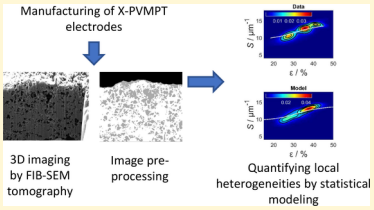

Electrochemical energy storage is of increasing relevance in today's technology-driven world with an ever-rising global demand for batteries. This includes electromobility and consumer electronics but also stationary grid-storage, where low-cost and safer alternatives to the lithium-ion battery might be future technologies. Organic electrode-active materials (OAMs) are attractive candidates for alternative battery concepts, made from more abundant elements,[1] being potentially cheaper and safer, and enabling a variety of charge (and concurrent ion) storage mechanisms.[2−4] Functioning under uptake of electrolyte (metal) cations (for n-type OAMs) or anions (p-type OAMs), OAMs can be used as a replacement for metal oxides in classical metal-ion batteries[5] but also function well with multivalent metal ions,[6−8] as well as in anionic cell configurations.[9] Poly(3-vinyl-*N*-methylphenothiazine) (PVMPT) or its cross-linked form X-PVMPT are high-performance p-type OAMs that enable fast and reversible energy storage (under anion insertion) in batteries at a high potential of 3.5 V vs Li/Li^+.[10] The charge-storage mechanism,[11,12] an effect of electrolyte type[13] and conductive carbon additive were studied in detail for PVMPT.[14] Due to its diminished solubility in liquid battery electrolytes,[15] cross-linked X-PVMPT is a particularly relevant OAM for full cells and showed exceptional performance in Al-based batteries,[16] surpassing graphite in specific capacity with high rate performance, as well as in an all-organic anion-rocking chair battery.[17] Structural engineering by changing the polymer backbone[18] affects the solubility[19] and charge-storage mechanism as well as the rate capability,[19,20] processing abilities,[21] and applicability[22−24] of phenothiazine-based redox polymers.[25]

Decisive for the performance of an OAM is not only its molecular or polymer structure but also to a large extent the morphology of the composite electrode used in the battery. The composite electrode consists of the OAM as well as a conductive carbon additive and binder. Its morphology strongly influences electron as well as ion transport, affecting the charge-storage performance. We herein investigate an X-PVMPT-based composite electrode with respect to the 3D morphology of its nanopores. For this purpose, 3D imaging is combined with methods from spatial statistics, mathematical morphology, and machine learning in order to quantify the

Received: July 30, 2024
Revised: April 3, 2025
Accepted: April 4, 2025
Published: April 17, 2025

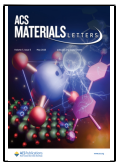

nanostructure of the considered X-PVMPT-based composite electrode. This allows us to locally evaluate porosity or surface area per unit volume, as well as to determine morphological descriptors, which are not accessible experimentally. For polymer-based battery electrodes, this approach has been used to elucidate morphological differences between PTMA, i.e., poly(2,2,6,6-tetramethyl-4-piperinidyl-*N*-oxyl methacrylate)-based, electrodes manufactured either with polyvinylidene fluoride (PVDF) or with water-soluble binder.[26] Recently, this methodology also revealed the impact of cross-linking in PTMA-CMK8 electrodes on their morphology.[27] In both studies, the morphology on the micrometer scale was quantified based on 3D image data acquired by synchrotron-tomography.[28,29]

In this paper, we consider the 3D morphology of an X-PVMPT electrode on the nanometer scale. Thus, focused ion beam−scanning electron microscopy (FIB-SEM)[30,31] is used for image acquisition, which allows for a voxel resolution of 10 nm. As in previous work,[27] image segmentation is performed by machine learning using the software ilastik.[32] The focus of the subsequent statistical image analysis is the quantification of local heterogeneities. Going beyond descriptive analyses,[26,27] we use parametric statistics to model the univariate distribution of local morphological descriptors and bivariate distributions of pairs of such descriptors. In doing so, the heterogeneity of the complex nanoporous morphology is characterized by a small number of model parameters. Moreover, by parametric modeling of the bivariate distributions, we obtain analytical formulas for the corresponding conditional distributions, such as, e.g., the distribution of the local surface area per unit volume conditioned on a predefined value of local porosity. From the conditional distributions, in turn, one can easily derive the corresponding expectations, variances, or quantiles, which elucidate quantitative relationships between pairs of local morphological descriptors. For this modeling approach we build upon methodologies previously developed for quantifying the 3D morphology of paper-based materials.[33,34] Furthermore, structural gradients within the X-PVMPT-based composite electrode considered in this paper are revealed.

Description of Electrode Material. The cross-linked X-PVMPT polymer with 10 mol % of the cross-linker was synthesized using the same procedure as previously reported.[15,16] Composite electrodes were prepared using 50 wt % X-PVMPT, 45 wt % carbon additive (Super C65, Timcal) and 5 wt % PVDF (Kynar HSV 900, Arkema). X-PVMPT and carbon black were pre-dried in a vacuum oven (10^{-3} mbar) at 60 °C for 24 h, then premixed using a planetary centrifugal mixer (1500 rpm, 15 min, ARM 310, Thinky mixer). The binder was added as a 5 wt % PVDF in *N*-methyl-2-pyrrolidone (NMP, Acroseals, Thermo Scientific, 99.5%, stored over molecular sieves) solution, and the composite was mixed. Finally, stepwise NMP additions and mixing steps (1500 rpm, 15 min) were performed until a honey-like viscosity was obtained. The resulting paste was blade-coated onto KOH-etched aluminum foil (1235 aluminum foil, H18 hard state, 20 μm from Gelon LIB), with a wet-film thickness of 100 μm. The coated foil was dried at ambient pressure at 60 °C for 24 h, and electrodes with a diameter of 12 mm were punched out with an electrode-punching device (EL-Cut from EL-CELL). The active material (X-PVMPT) mass loadings of the electrodes lie between 0.22 and 0.24 mg cm^{-2}. Note that the theoretical specific capacity of X-PVMPT for a one-electron process is 112 mAh/g, while the practical capacity lies close to this value in Li half cells.[15]

3D Imaging by FIB-SEM Tomography. For 3D tomography using FIB-SEM, the polymer sample was first mounted on a standard 12.5 mm aluminum SEM stub. For this purpose, a 1 mm × 3 mm piece was cut out with a scalpel and glued to the SEM holder with the aluminum conductor side using a carbon adhesive pad. Copper tape was glued over one side of the sample to ensure good conductivity of the sample during SEM imaging. The sample was then inserted into the ZEISS Crossbeam 340 of the Corelab Correlative Microscopy and Spectroscopy (CCMS) at Helmholtz-Zentrum Berlin (HZB). Using a gallium ion beam current of 15 nA (at 30 keV), the polymer material and parts of the underlying aluminum conductor were first removed in a 30 μm × 30 μm area in the center of the polymer sample. The cross-section exposed for imaging was polished with an ion current of 300 pA. A low acceleration voltage of 1 keV was used for imaging to minimize the depth of the electron penetration into the sample. An image size of 2048 pixels × 1536 pixels was selected for imaging with an acquisition time of 20.5 s per image. A chamber mounted SE2 detector was used for serial imaging. With a field of view of 20.5 μm, this resulted in a pixel size of 10 nm. The ion beam was then used to remove a 10 nm layer of the sample between each image using a 300 pA current at 30 keV, resulting in a 3D data set with an isotropic voxel edge length of 10 nm.

Preprocessing and Segmentation of Image Data. The porous nanostructure of the X-PVMPT-based electrode material was reconstructed from grayscale 3D FIB-SEM data by a phase-based segmentation, which required data preprocessing. First, a drift correction was applied. This was done by registering the areas above the current cross-section. These areas had not yet been cut by the gallium beam and therefore contained image information about the surface of the unaltered sample. Therefore, features detected in these areas had to be constantly moving toward the cutting edge of the forward moving cross-section. Any nonconstant motion was corrected using the scale-invariant feature transform (SIFT) algorithm,[35] implemented in FIJI.[36] Subsequently, the sample is aligned to the coordinate system of the sampling window, as shown in Figure 1. The *x*-axis goes from left to right, the *z*-axis from bottom to top, and the *y*-axis goes through the image slices starting at the first image slice.

To analyze the nanostructure of the electrode, a phase-based segmentation of the grayscale FIB-SEM data was performed. This means that each voxel of the image is assigned to either solid, pores, or background. Note, however, that the electrode material depicted in the image data has a large diagonal crack, see Figure 1. This is problematic not only in terms of

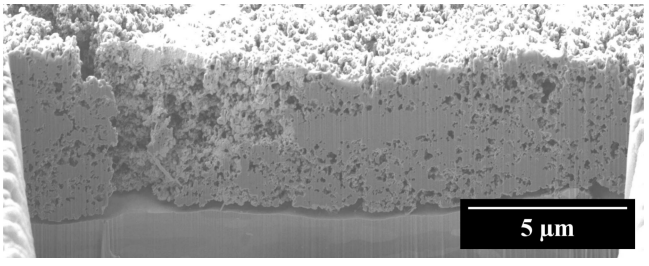

Figure 1. 2D slice of grayscale image data obtained by FIB-SEM tomography.

https://doi.org/10.1021/acsmaterialslett.4c01552
ACS Materials Lett. 2025, 7, 1914−1921

segmentation but also for the subsequent statistical analysis. Therefore, only a cutout, visualized in Figure 2a, was used for statistical image analysis. For segmentation of the cutout, a random forest classifier[37] was trained with hand-labeled data, using the software ilastik.[32] Two hand-labeled slices are shown in Figure 2c,d, which are orthogonal to each other. Details are provided in the Supporting Information. Finally, to distinguish between background and pores in the complement of the solid phase, a so-called rolling ball algorithm[38] with a radius of 20 voxels (0.2 μm) has been used, which was previously applied for PTMA-based battery electrodes.[26,27] A 2D slice of the final segmentation is shown in Figure 2b.

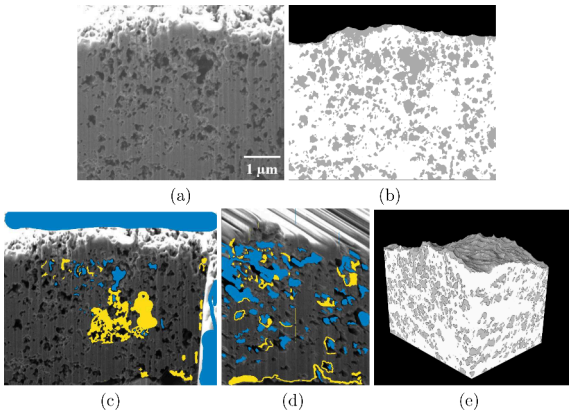

Figure 2. Cutout of FIB-SEM image data (a); corresponding 2D slice of segmentation into solid phase (white), pores (gray), and background (black) (b); hand-labeling of image data: blue color represents background and pores, whereas yellow represents the solid phase (c, d); and 3D rendering of the segmented image data (e).

Morphological Descriptors. Using tools of statistical image analysis, the segmentation of image data into solid and pore phases allows for the quantitative characterization of electrode nanostructures and, in particular, local heterogeneities thereof. For this purpose, morphological descriptors of the nanostructure are globally and locally evaluated. The morphological descriptors considered in the present paper are the thickness δ, the porosity ε, the surface area between solid and pore phases per unit volume S, as well as the mean geodesic tortuosity[39] of the solid and pore phases, denoted by τ_s and τ_p, respectively. The considered descriptors are crucial for battery electrodes since thickness influences the capacity of the electrode and electrochemical reactions take place at the surface area, while porosity and mean geodesic tortuosities strongly influence effective transport properties such as effective ionic diffusivity and effective electric conductivity.[40,41]

Global morphological descriptors are computed based on the complete image as a sampling window. For the computation of local descriptors, we consider nonoverlapping square-shaped cutouts with side length of 1 μm, the centers of which are arranged on a regular hexahedral grid, in the plane parallel to the aluminum foil. For each of these cutouts, the above-mentioned morphological descriptors are determined, where the full thickness is taken into account. In doing so, we follow previous approaches for investigating local heterogeneities.[26,27,33,34] Then, we get empirical distributions of local morphological descriptors, which are parametrically modeled. Details on the computation of morphological descriptors are provided in the Supporting Information.

Parametric Statistical Modeling of Local Morphological Descriptors. For each descriptor, we consider various families of parametric distributions as candidates. For each of these families, parameter fitting is performed by maximum likelihood estimation. Based on Akaike's information criterion,[42] we choose the distribution type from all candidate families of distributions. In this way, for the five local morphological descriptors mentioned above, we selected a Maxwell−Boltzmann distribution $\mathrm{MB}(\mu_M, \sigma_M)$, Rayleigh distribution $R(\mu_R, \sigma_R)$ and shifted Gamma distribution $\Gamma(a_\Gamma, \sigma_\Gamma, \mu_\Gamma)$, as well as mixtures of Gaussian and Beta distributions, denoted by $N(\mu_1, \mu_2, \sigma_1, \sigma_2, p_N)$ and $\mathrm{Beta}(\alpha_1, \alpha_2, \beta_1, \beta_2, p_B)$ for parameters $\mu_M, \mu_R, \mu_\Gamma, \mu_1, \mu_2 \in \mathbb{R}$, $\sigma_M, \sigma_R, a_\Gamma, \sigma_\Gamma, \sigma_1, \sigma_2, \beta_1, \beta_2 > 0$ and $0 \leq p_N, p_B \leq 1$. The probability density functions of these distributions are provided in the Supporting Information. The fitted parameters are presented in Table 3.

The bivariate probability densities of descriptor pairs could simply be modeled as products of the corresponding univariate densities. However, this would require that the underlying local morphological descriptors would not be (or at least be only weakly) correlated. But this is not the case, as can be seen in Table 1. Moreover, in most cases, the univariate densities are not Gaussian; see Figure 4. Therefore, the bivariate probability densities of descriptor pairs are modeled by means of so-called copulas.[33] This approach is advantageous in the sense that the complexity of the model is split into modeling the univariate marginal distributions and modeling the copula, where the copula contains information about the interdependence of the individual morphological descriptors.

Table 1. Correlation Matrix of Local Morphological Descriptors ε, δ, S, τ_s and τ_p

	ε	δ	S	τ_s	τ_p
ε	1.0	0.55	0.86	−0.59	0.80
δ		1.0	0.58	−0.48	0.46
S			1.0	−0.64	0.59
τ_s				1.0	−0.46
τ_p					1.0

For modeling the bivariate probability densities of descriptor pairs consisting of local porosity and one of the remaining four morphological descriptors, we consider one-parametric Archimedean copulas[43] as the model type. In all four cases the best fit was obtained by a Frank copula C: $[0, 1]^2 \to [0, 1]$, defined by

$$C(u, v) = -\frac{1}{\theta}\log\left(1 + \frac{(\mathrm{e}^{-\theta u} - 1)(\mathrm{e}^{-\theta v} - 1)}{\mathrm{e}^{-\theta} - 1}\right)$$

for any $u, v \in [0, 1]$, where $\theta \in \mathbb{R}\backslash\{0\}$ is some model parameter. Plugging the parametric distribution functions and probability densities of the univariate distributions as well as the parametric copula into the formulas for conditional probability densities, we obtained analytical formulas for the latter ones. These analytical formulas fully quantify the relationship between pairs of local morphological descriptors. In particular, they can be used to compute conditional expectations and quantiles of a morphological descriptor for a fixed porosity. The latter can be used for predictions of local morphological descriptors based on local porosity.

https://doi.org/10.1021/acsmaterialslett.4c01552
ACS Materials Lett. 2025, 7, 1914−1921

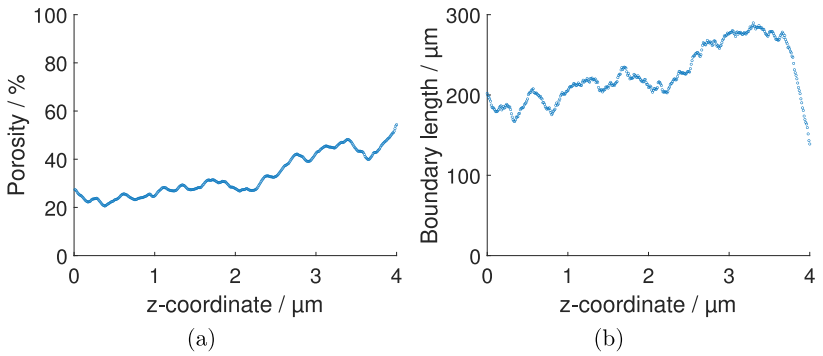

Figure 3. Dependence of porosity (a) and boundary length (b) on the height z within the electrode.

RESULTS

From visual inspection of the cutout shown in Figure 2a, it seems that the porosity of the sample depends on the height, i.e., the z-value of the location we look at. This is confirmed by the results of statistical image analysis, when we determine porosity and boundary length of the interface between pores and solid at a given height $z \in [0, 4]$ μm; see Figure 3. Note that for this purpose we consider the complete sample in the xy-plane. Here we can see that both characteristics strongly depend on the z-position, as porosity and boundary length increase approaching the top part of the electrode.

Furthermore, the spatial gradient of the boundary length presented in Figure 3 shows that the surface area per unit volume in 3D is increasing with increasing distance to the aluminum foil. This observation is in good accordance with the spatial gradient observed for porosity as, depending on the shape of the phases, the surface area typically takes its maximum when both phases, pores and solid, have nearly the same volume fraction. For certain PTMA-based electrodes, for example, the surface area per unit volume on the microscale takes its maximum at a volume fraction of PTMA at 60%.[26] The values of global morphological descriptors for the X-PVMPT-based composite electrode considered in this paper, which have been obtained by averaging over results for all sampling windows, are given in Table 2.

Table 2. Global Morphological Descriptors, Obtained by Averaging over Results for All Sampling Windows

ε	δ	S	τ_s	τ_p
37%	4.02 μm	8.82 μm^{-1}	1.04	1.24

To investigate local heterogeneities of the X-PVMPT-based composite electrode, we first computed the values of ε, δ, S, τ_s, and τ_p for each of the nonoverlapping square-shaped cutouts with side length of 1 μm. The corresponding empirical distributions were obtained by kernel density estimation by using a Gaussian kernel. The fitted parametric families of distributions and the corresponding parameter values are summarized in Table 3. Note that in the following figures, the empirical distributions are referred to as "data", while the fitted parametric univariate distributions are referred to as "model".

We first consider the empirical probability density of the local thickness δ, which is shown in Figure 4a. There is only a little variability visible for δ, being almost symmetrically distributed around the mean. As a parametric model, a Maxwell−Boltzmann distribution was fitted. Looking at the results obtained for porosity ε, see Figure 4b, a bimodal density can be observed. The modes are located at 23% and 35%, respectively, where the distribution is less concentrated at the latter. The values of ε vary from 15% up to 50%, which shows a strong heterogeneity of local porosity. Considering the porosity ε as a volume fraction, it takes values between 0 and 1. Thus, keeping in mind that the kernel density estimate of ε is bimodal, we have chosen a mixture of two Beta distributions as a parametric model.

The shape of the density of the local surface area S, visible in Figure 4c, results from the correlation between the volume fraction and surface area per unit volume, also discussed in the context of the spatial gradients shown in Figure 3. The surface area per unit volume tends to take its maximum in the case that the fractions of solid and pores are nearly identical. Because of this interdependence of local porosity ε and local specific surface area S and in view of the bimodality of the density of ε, a bimodal parametric model, namely a mixture of two Gaussian distributions, was chosen for S.

The empirical density of the mean geodesic tortuosity τ_s in the solid phase is shown in Figure 4e. For large parts of the electrode, straight pathways in the solid phase with almost no obstruction from the top- to the bottom-face of the electrode can be found. This results in a distribution, which is mainly concentrated at small tortuosity values of about 1.04. Note that for PTMA-CMK8 electrodes, comparably short, or even shorter, transportation pathways are observed in the solid phase at the microscale.[27] Compared to nanostructured $LiNi_{1/3}Mn_{1/3}Co_{1/3}Co_2$ (NMC) active material particles, 1.04 is rather low. For differently manufactured nanostructured

Table 3. Morphological Descriptors, Fitted Parametric Distribution Types, and Parameter Values

descriptor	distribution type	parameter values
ε	Beta mixture	$\alpha_1 = 109.43$, $\alpha_2 = 125.79$, $\beta_1 = 65.44$, $\beta_2 = 47.74$, $p_B = 0.59$
δ	Maxwell−Boltzmann	$\mu_M = 3.46$, $\sigma_M = 0.35$
S	Gaussian mixture	$\mu_1 = 13.1$, $\mu_2 = 10.46$, $\sigma_1 = 0.87$, $\sigma_2 = 1.06$, $p_N = 0.56$
τ_s	Rayleigh	$\mu_R = 1.01$, $\sigma_R = 0.024$
τ_p	Gamma	$a_\Gamma = 2.97$ $\mu_\Gamma = 1.14$, $\sigma_\Gamma = 0.037$

https://doi.org/10.1021/acsmaterialslett.4c01552
ACS Materials Lett. 2025, 7, 1914−1921

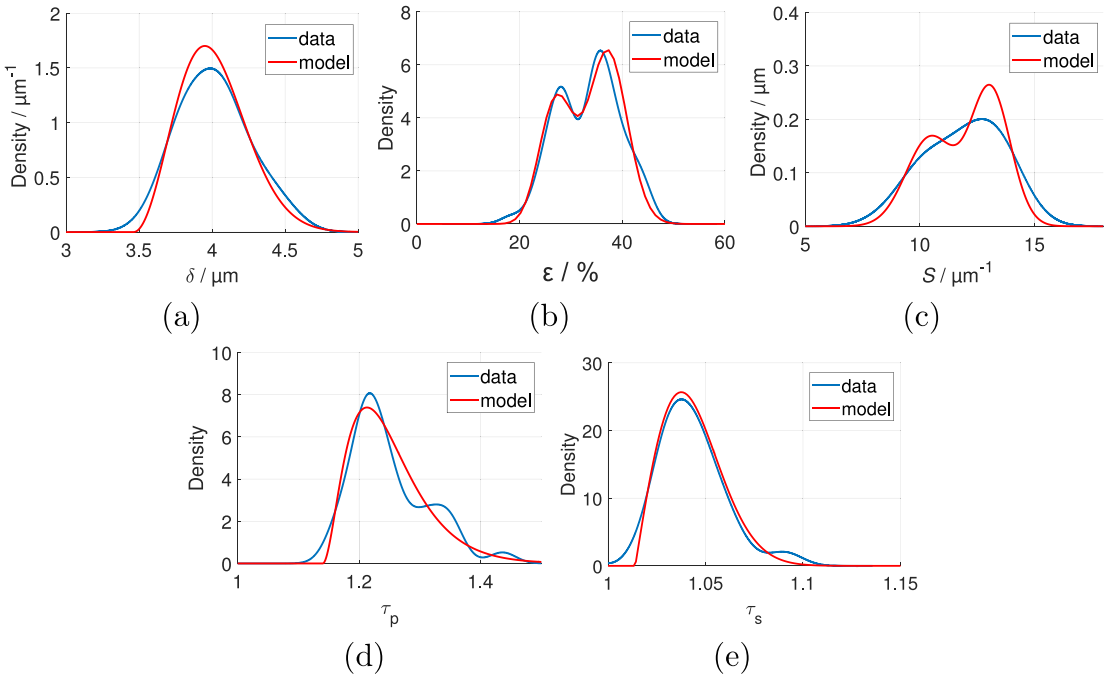

Figure 4. Empirical probability density (data) and fitted parametric density (model) of local thickness δ (a), local porosity ε (b), local surface area per unit volume S (c), and mean geodesic tortuosities, τ_p and τ_s, in the pore phase (d) and solid phase (e), respectively.

NMC particles, the mean geodesic tortuosity of solid and pores exceeds 1.04.[44] Nevertheless, in the present paper, τ_s still locally reaches values of up to 1.1. This could be explained by the higher porosity in certain areas, which leads to fewer pathways in the solid phase and, therefore, to larger values of τ_s. Thus, a Rayleigh distribution[45] was used for the fitting of a parametric model. Moreover, the empirical density of mean geodesic tortuosity of the pore phase τ_p, depicted in Figure 4d, was analyzed. This descriptor is of even higher importance than the mean geodesic tortuosity in the solid phase τ_s since the supply of electrons in the solid phase is rarely a limiting factor regarding the electrochemical performance of electrodes. The values of τ_p range from 1.15 up to 1.5 with the highest concentration at about 1.22. This effect can again be explained by the local behavior of porosity since there are in general much fewer possible pathways in the pore space, increasing the shortest path length and therefore increasing the mean geodesic tortuosity τ_p. It turned out that a Gamma distribution fits the empirical density of τ_p quite well; see Figure 4d.

In order to model the bivariate distribution of descriptor pairs, consisting of ε and one of the remaining descriptors δ, S, τ_s, and τ_p, we use the fitted univariate models and additionally fit the parameter of the Frank copula; see Table 4. Comparing the model with the corresponding bivariate empirical distributions shows a nice fit; see Figure 5.

Table 4. Fitted Parameters of the Frank Copula for Descriptor Pairs, Where the First Descriptor Is the Porosity ε

second descriptor	fitted parameter of Frank copula
δ	$\theta = 4.09$
S	$\theta = 9.77$
τ_s	$\theta = 8.89$
τ_p	$\theta = -4.96$

By visual inspection of the bivariate densities shown in Figure 5, it becomes evident that the local porosity ε is correlated with the remaining four descriptors δ, S, τ_s, and τ_p. Regarding the pair (ε, δ) of thickness and porosity, considered in Figure 5a,e, we can see that these two descriptors are positively correlated, see also Table 1. This behavior is sensible in the way that the electrode seems to be thicker in the center of the image data cutout, where we also observed large porous regions compared to other parts of the data; see Figure 2b.

Furthermore, looking at the bivariate density of (ε, S), i.e., local porosity and surface area per unit volume, presented in Figure 5b,f, we also observe a positive correlation. On the other hand, the bivariate density of (ε, τ_p), i.e., porosity and mean geodesic tortuosity of the pore phase, shown in Figure 5c,g, indicates a negative correlation. This is not surprising since decreasing the porosity means less pore space and, therefore, fewer pathways that can be traversed, which results in longer pathways and consequently increases the mean geodesic tortuosity of the pore space. With similar arguments as those above, the positive correlation of (ε, τ_s), i.e., local porosity and mean geodesic tortuosity of the solid phase, can be explained. Decreasing porosity increases the volume fraction of the solid phase and, thus, the number of possible pathways through the solid phase, which decreases the average length of the shortest pathways in this phase.

DISCUSSION

The 3D morphology of the X-PVMPT-based composite electrode investigated in this work shows two different types of structural heterogeneity. On the one hand, we observed that the porosity of the sample is highly dependent on the z-position in the electrode, meaning that the electrode material is more porous near the top-face. These porous regions at the top also have coarser surfaces since the boundary area of the solid phase is larger at the top-face of the electrode; see Figure 3. These spatial gradients might presumably arise during the

https://doi.org/10.1021/acsmaterialslett.4c01552
ACS Materials Lett. 2025, 7, 1914−1921

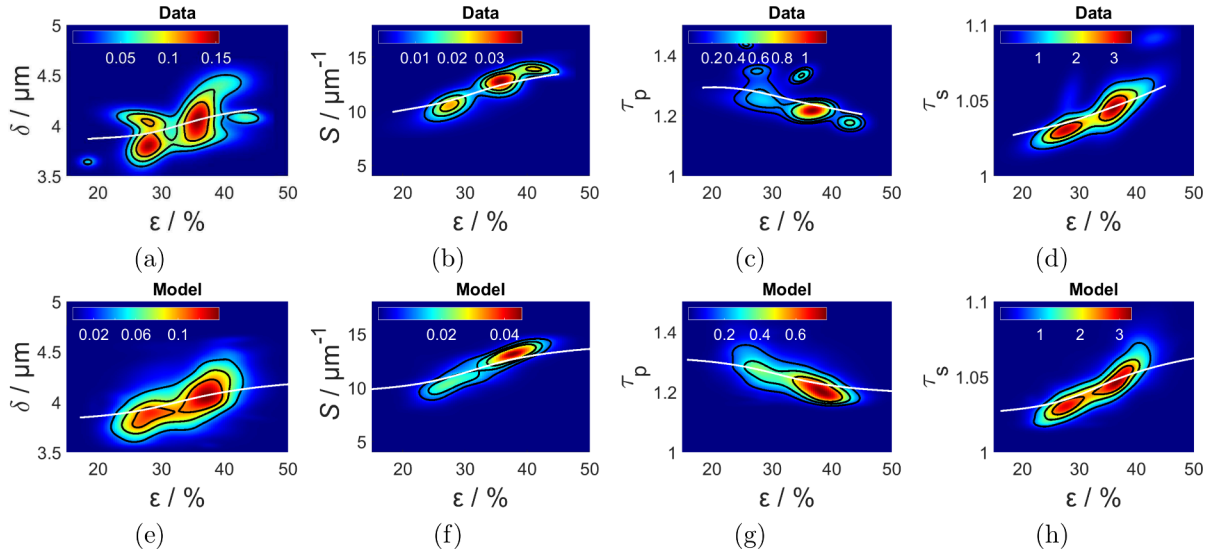

Figure 5. Bivariate empirical densities (top row) and fitted parametric densities (bottom row) of pairs of local microstructure descriptors. The bivariate probability densities are visualized as heat maps, where the white lines represent the (conditional) mean values for given local porosities. The black contour lines are the 25%, 50%, and 75% quantiles, respectively.

drying process. In order to support this conjecture and to achieve a detailed understanding of the relationships between process parameters and the gradient of porosity, further research is required including 3D imaging of differently manufactured X-PVMPT electrodes.

On the other hand, we observed considerable local heterogeneities of the electrode material for different 3D cutouts along the *xy*-plane. This can be seen by the high variances in the univariate distributions of the local morphological descriptors fitted to segmented image data. Furthermore, we observed a positive correlation between local porosity ε and thickness δ as well as between ε and surface area per unit volume S. However, note that the values of local thickness δ of the electrode material show relatively little variation and are pretty closely grouped around their mean value; see Figure 4a. The mean geodesic tortuosity of the solid phase τ_s showed values close to 1, which implicates short transportation paths through the solid phase. In contrast, we have seen that the mean geodesic tortuosity of the pore phase τ_p exhibits larger values, which tells us that the paths through the porous phase are much more winded.

CONCLUSION

Our analysis of the X-PVMPT-based composite electrodes provides valuable insights into the nanostructural properties and local heterogeneities of their 3D morphology. The combination of FIB-SEM tomography, which achieved a voxel resolution of 10 nm, and image segmentation techniques allowed for detailed morphological characterization of the electrode. The investigations performed in this study focused on key morphological descriptors such as thickness, porosity, surface area per unit volume, and mean geodesic tortuosity for both solid and pore phases. These descriptors are crucial to the performance of the electrode. In particular, the porosity was observed to be highly variable and dependent on the *z*-position within the electrode, with higher porosity and coarser surfaces toward the top. This heterogeneity was further supported by the distributions of local descriptors, which were modeled by using parametric probability distributions. The bivariate densities, modeled with Frank copulas, revealed quantitative relationships between descriptors, especially the correlations between porosity and the remaining four morphological descriptors. Notably, the values obtained for the local mean geodesic tortuosities τ_s and τ_p indicated that pathways through the solid phase were relatively straight, whereas those through the pore phase were more winded, impacting the overall charge-transport properties through these two phases. These insights emphasize the critical role of the nanostructure with respect to the performance of organic electrode-active materials (OAMs). Understanding and controlling these morphological features can pave the way for optimizing battery design for X-PVMPT electrodes and enhancing the efficiency of polymer-based batteries, as was already done for NMC-based electrodes.[46] The results obtained in this paper provide a foundation for future research on the morphological optimization of OAM-based electrodes, contributing to the advancement of safer, more efficient, and cost-effective battery technologies.

ASSOCIATED CONTENT

Supporting Information

The Supporting Information is available free of charge at https://pubs.acs.org/doi/10.1021/acsmaterialslett.4c01552.

Additional details related to image segmentation, computation of morphological descriptors, univariate probability density functions used in the present paper, and a brief introduction to copulas (PDF)

AUTHOR INFORMATION

Corresponding Author

Matthias Neumann − *Institute of Statistics, Graz University of Technology, 8010 Graz, Austria;* orcid.org/0000-0002-5782-6773; Email: neumann@tugraz.at

Authors

Lukas Dodell − *Institute of Stochastics, Ulm University, 89069 Ulm, Germany*

https://doi.org/10.1021/acsmaterialslett.4c01552
ACS Materials Lett. 2025, 7, 1914−1921

Markus Osenberg − *Institute of Applied Materials, Helmholtz Zentrum für Materialien und Energie, 14109 Berlin, Germany*
André Hilger − *Institute of Applied Materials, Helmholtz Zentrum für Materialien und Energie, 14109 Berlin, Germany*
Gauthier Studer − *Institute of Organic Chemistry II and Advanced Materials, Ulm University, 89069 Ulm, Germany*
Birgit Esser − *Institute of Organic Chemistry II and Advanced Materials, Ulm University, 89069 Ulm, Germany;* orcid.org/0000-0002-2430-1380
Ingo Manke − *Institute of Applied Materials, Helmholtz Zentrum für Materialien und Energie, 14109 Berlin, Germany;* orcid.org/0000-0001-9795-5345
Volker Schmidt − *Institute of Stochastics, Ulm University, 89069 Ulm, Germany*

Complete contact information is available at: https://pubs.acs.org/10.1021/acsmaterialslett.4c01552

Author Contributions

[▽]L.D. and M.N. contributed equally to this paper.

Notes

The authors declare no competing financial interest.

■ ACKNOWLEDGMENTS

This research has been supported by the German Research Foundation (DFG) under Grants 441292784 and 441215516, within Priority program 2248 "Polymer-based batteries" of DFG. Moreover, this research was funded by DFG under Project ID 390874152 (POLiS Cluster of Excellence, EXC 2154). The present paper contributes to the research performed at CELEST (Center for Electrochemical Energy Storage Ulm-Karlsruhe).

■ REFERENCES

(1) Kim, J.; Kim, Y.; Yoo, J.; Kwon, G.; Ko, Y.; Kang, K. Organic batteries for a greener rechargeable world. *Nature Reviews Materials* **2023**, *8*, 54−70.
(2) Esser, B. Redox polymers as electrode-active materials for batteries. *Organic Materials* **2019**, *01*, 063−070.
(3) Esser, B.; Dolhem, F.; Becuwe, M.; Poizot, P.; Vlad, A.; Brandell, D. A perspective on organic electrode materials and technologies for next generation batteries. *Power Sources* **2021**, *482*, 228814.
(4) Poizot, P.; Gaubicher, J.; Renault, S.; Dubois, L.; Liang, Y.; Yao, Y. Opportunities and challenges for organic electrodes in electrochemical energy storage. *Chem. Rev.* **2020**, *120*, 6490−6557.
(5) Yang, H.; Lee, J.; Cheong, J. Y.; Wang, Y.; Duan, G.; Hou, H.; Jiang, S.; Kim, I.-D. Molecular engineering of carbonyl organic electrodes for rechargeable metal-ion batteries: fundamentals, recent advances, and challenges. *Energy Environ. Sci.* **2021**, *14*, 4228−4267.
(6) Huang, Z.; Du, X.; Ma, M.; Wang, S.; Xie, Y.; Meng, Y.; You, W.; Xiong, L. Organic cathode materials for rechargeable aluminum-ion batteries. *ChemSusChem* **2023**, *16*, 637−671.
(7) Li, Z.; Häcker, J.; Fichtner, M.; Zhao-Karger, Z. Cathode materials and chemistries for magnesium batteries: challenges and opportunities. *Adv. Energy Mater.* **2023**, *13* (27), 2300682.
(8) Chen, Y.; Fan, K.; Gao, Y.; Wang, C. Challenges and perspectives of organic multivalent metal-ion batteries. *Adv. Mater.* **2022**, *34*, 2200662.
(9) Poizot, P.; Dolhem, F.; Gaubicher, J. Progress in all-organic rechargeable batteries using cationic and anionic configurations: toward low-cost and greener storage solutions? *Current Opinion in Electrochemistry* **2018**, *9*, 70−80.
(10) Kolek, M.; Otteny, F.; Schmidt, P.; Mück-Lichtenfeld, C.; Einholz, C.; Becking, J.; Schleicher, E.; Winter, M.; Bieker, P.; Esser, B. Ultra-high cycling stability of poly(vinylphenothiazine) as a battery cathode material resulting from π-π interactions. *Energy Environ. Sci.* **2017**, *10*, 2334−2341.
(11) Kolek, M.; Otteny, F.; Becking, J.; Winter, M.; Esser, B.; Bieker, P. Mechanism of charge/discharge of poly(vinylphenothiazine)-based li−organic batteries. *Chem. Mater.* **2018**, *30*, 6307−6317.
(12) Otteny, F.; Perner, V.; Einholz, C.; Desmaizieres, G.; Schleicher, E.; Kolek, M.; Bieker, P.; Winter, M.; Esser, B. Bridging the gap between small molecular π-interactions and their effect on phenothiazine-based redox polymers in organic batteries. *ACS Applied Energy Materials* **2021**, *4*, 7622−7631.
(13) Perner, V.; Diddens, D.; Otteny, F.; KüPers, V.; Bieker, P.; Esser, B.; Winter, M.; Kolek, M. Insights into the solubility of poly(vinylphenothiazine) in carbonate-based battery electrolytes. *ACS Appl. Mater. Interfaces* **2021**, *13*, 12442−12453.
(14) Tengen, B.; Winkelmann, T.; Ortlieb, N.; Perner, V.; Studer, G.; Winter, M.; Esser, B.; Fischer, A.; Bieker, P. Immobilizing poly(vinylphenothiazine) in ketjenblack-based electrodes to access its full specific capacity as battery electrode material. *Adv. Funct. Mater.* **2023**, *33*, 2210512.
(15) Otteny, F.; Kolek, M.; Becking, J.; Winter, M.; Bieker, P.; Esser, B. Unlocking full discharge capacities of poly(vinylphenothiazine) as battery cathode material by decreasing polymer mobility through cross-linking. *Adv. Energy Mater.* **2018**, *8*, 1802151.
(16) Studer, G.; Schmidt, A.; Büttner, J.; Schmidt, M.; Fischer, A.; Krossing, I.; Esser, B. On a high-capacity aluminium battery with a two-electron phenothiazine redox polymer as a positive electrode. *Energy Environ. Sci.* **2023**, *16*, 3760−3769.
(17) Bhosale, M.; Schmidt, C.; Penert, P.; Studer, G.; Esser, B. Anion-rocking chair batteries with tuneable voltage using viologen- and phenothiazine polymer-based electrodes. *ChemSusChem* **2024**, *17*, No. e202301143.
(18) Desmaizieres, G.; Perner, V.; Wassy, D.; Kolek, M.; Bieker, P.; Winter, M.; Esser, B. Evaluating the polymer backbone − vinylene versus styrene − of anisyl-substituted phenothiazines as battery electrode materials. *Batteries & Supercaps* **2023**, *6*, No. e202200464.
(19) Otteny, F.; Studer, G.; Kolek, M.; Bieker, P.; Winter, M.; Esser, B. Phenothiazine-functionalized poly(norbornene)s as high-rate cathode materials for organic batteries. *ChemSusChem* **2020**, *13*, 2232−2238.
(20) Acker, P.; Rzesny, L.; Marchiori, C.r F. N.; Araujo, C. M.; Esser, B. π-conjugation enables ultra-high rate capabilities and cycling stabilities in phenothiazine copolymers as cathode-active battery materials. *Adv. Funct. Mater.* **2019**, *29*, 1906436.
(21) Acker, P.; Wössner, J. S.; Desmaizieres, G.; Esser, B. Conjugated copolymer design in phenothiazine-based battery materials enables high mass loading electrodes. *ACS Sustainable Chem. Eng.* **2022**, *10*, 3236−3244.
(22) Wessling, R.; Delgado Andrés, R.; Morhenn, I.; Acker, P.; Maftuhin, W.; Walter, M.; Würfel, U.; Esser, B. Phenothiazine-based donor−acceptor polymers as multifunctional materials for charge storage and solar energy conversion. *Macromol. Rapid Commun.* **2024**, *45*, 2200699.
(23) Delgado Andrés, R.; Wessling, R.; Büttner, J.; Pap, L.; Fischer, A.; Esser, B.; Würfel, U. Organic photo-battery with high operating voltage using a multi-junction organic solar cell and an organic redox-polymer-based battery. *Energy Environ. Sci.* **2023**, *16*, 5255−5264.
(24) Wessling, R.; Koger, H.; Otteny, F.; Schmidt, M.; Semmelmaier, A.; Esser, B. Unlocking twofold oxidation in phenothiazine polymers for application in symmetric all-organic anionic batteries. *ACS Applied Polymer Materials* **2024**, *6*, 7956−7968.
(25) Otteny, F.; Desmaizieres, G.; Esser, B. Phenothiazine-based redox polymers for energy storage. In *Redox Polymers for Energy and Nanomedicine*; The Royal Society of Chemistry, 2020; pp 166−197.
(26) Neumann, M.; Ademmer, M.; Osenberg, M.; Hilger, A.; Wilde, F.; Muench, S.; Hager, M. D.; Schubert, U. S.; Manke, I.; Schmidt, V. 3D microstructure characterization of polymer battery electrodes by statistical image analysis based on synchrotron x-ray tomography. *J. Power Sources* **2022**, *542*, 231783.

(27) Ademmer, M.; Su, P.-H.; Dodell, L.; Asenbauer, J.; Osenberg, M.; Hilger, A.; Chang, J.-K.; Manke, I.; Neumann, M.; Schmidt, V.; Bresser, D. Unveiling the impact of crosslinking redox-active polymers on their electrochemical behavior by 3D imaging and statistical microstructure analysis. *J. Phys. Chem. C* **2023**, *127*, 19366−19377.
(28) Heenan, T. M. M.; Tan, C.; Hack, J.; Brett, D. J. L.; Shearing, R. P. Developments in X-ray tomography characterization for electrochemical devices. *Mater. Today* **2019**, *31*, 69−85.
(29) Tang, F.; Wu, Z.; Yang, C.; Osenberg, M.; Hilger, A.; Dong, K.; Markötter, H.; Manke, I.; Sun, F.; Chen, L.; Cui, G. Synchrotron X-Ray tomography for rechargeable battery research: fundamentals, setups and applications. *Small Methods* **2021**, *5*, 2100557.
(30) Holzer, L.; Cantoni, M. Review of FIB-tomography. In *Nanofabrication using Focused Ion and Electron Beams: Principles and Applications*; Utke, I., Moshkalev, S., Russell, P., Eds.; Oxford University Press, 2012; pp 410−435.
(31) Möbus, G.; Inkson, B. J. Nanoscale tomography in materials science. *Mater. Today* **2007**, *10*, 18−25.
(32) Berg, S.; Kutra, D.; Kroeger, T.; Straehle, C. N.; Kausler, B. X.; Haubold, C.; Schiegg, M.; Ales, J.; Beier, T.; Rudy, M.; Eren, K.; Cervantes, J. I.; Xu, B.; Beuttenmueller, F.; Wolny, A.; Zhang, C.; Koethe, U.; Hamprecht, F. A.; Kreshuk, A. ilastik: interactive machine learning for (bio)image analysis. *Nat. Methods* **2019**, *16*, 1226−1232.
(33) Neumann, M.; Machado Charry, E.; Zojer, K.; Schmidt, V. On variability and interdependence of local porosity and local tortuosity in porous materials: a case study for sack paper. *Methodology and Computing in Applied Probability* **2021**, *23*, 613−627.
(34) Neumann, M.; Gräfensteiner, P.; Machado Charry, E.; Hirn, U.; Hilger, A.; Manke, I.; Schennach, R.; Schmidt, V.; Zojer, K. R-vine copulas for data-driven quantification of descriptor relationships in porous materials. *Advanced Theory and Simulations* **2024**, *7*, 2301261.
(35) Lowe, D. G. Distinctive image features from scale-invariant keypoints. *International Journal of Computer Vision* **2004**, *60*, 91−110.
(36) Schindelin, J.; Arganda-Carreras, I.; Frise, E.; Kaynig, V.; Longair, M.; Pietzsch, T.; Preibisch, S.; Rueden, C.; Saalfeld, S.; Schmid, B.; Tinevez, J.-Y.; White, D. J.; Hartenstein, V.; Eliceiri, K.; Tomancak, P.; Cardona, A. Fiji: an open-source platform for biological-image analysis. *Nat. Methods* **2012**, *9*, 676−682.
(37) Breiman, L. Random forests. *Machine Learning* **2001**, *45*, 5−32.
(38) Machado Charry, E.; Neumann, M.; Lahti, J.; Schennach, R.; Schmidt, V.; Zojer, K. Pore space extraction and characterization of sack paper using μ-CT. *J. Microsc.* **2018**, *272*, 35−46.
(39) Holzer, L.; Marmet, P.; Fingerle, M.; Wiegmann, A.; Neumann, M.; Schmidt, V. In *Tortuosity and Microstructure Effects in Porous Media: Classical Theories, Empirical Data and Modern Methods*; Springer, 2023.
(40) Neumann, M.; Stenzel, O.; Willot, F.; Holzer, L.; Schmidt, V. Quantifying the influence of microstructure on effective conductivity and permeability: virtual materials testing. *International Journal of Solid and Structures* **2020**, *184*, 211−220.
(41) Prifling, B.; Röding, M.; Townsend, P.; Neumann, M.; Schmidt, V. Large-scale statistical learning for mass transport prediction in porous materials using 90,000 artificially generated microstructures. *Frontiers in Materials* **2021**, *8*, 786502.
(42) Bozdogan, H. Model selection and Akaike's information criterion (AIC): The general theory and its analytical extensions. *Psychometrika* **1987**, *52*, 345−370.
(43) Nelsen, R. B. In *An Introduction to Copulas*; Springer, 2007.
(44) Neumann, M.; Wetterauer, S. E.; Osenberg, M.; Hilger, A.; Gräfensteiner, P.; Wagner, A.; Bohn, N.; Binder, J. R.; Manke, I.; Carraro, T.; Schmidt, V. A data-driven modeling approach to quantify morphology effects on transport properties in nanostructured NMC particles. *International Journal of Solids and Structures* **2023**, *280*, 112394.
(45) Siddiqui, M. M. Statistical inference for rayleigh distributions. *Journal of Research of the National Bureau of Standards* **1964**, *68D*, 1005−1010.
(46) Kremer, L. S.; Hoffmann, A.; Danner, T.; Hein, S.; Prifling, B.; Westhoff, D.; Dreer, C.; Latz, A.; Schmidt, V.; Wohlfahrt-Mehrens, M. Manufacturing process for improved ultra-thick cathodes in high-energy lithium-ion batteries. *Energy Technology* **2020**, *8*, 1900167.

https://doi.org/10.1021/acsmaterialslett.4c01552
ACS Materials Lett. 2025, 7, 1914−1921